Applied Catalysis B: Environmental 257 (2019) 117869

Contents lists available at ScienceDirect

Applied Catalysis B: Environmental

journal homepage: www.elsevier.com/locate/apcatb

# Surface charge-induced activation of Ni-loaded CdS for efficient and robust photocatalytic dehydrogenation of methanol

Hanlin Huang[a,b,d], Yu Jin[a,c,d], Zhigang Chai[a,b,d], Xianrui Gu[a,d], Yongqi Liang[a,b,d], Qi Li[a,b,d], Haichao Liu[a,d], Hong Jiang[a,c,d,*], Dongsheng Xu[a,b,d,*]

[a] College of Chemistry and Molecular Engineering, Peking University, Beijing 100871, PR China
[b] State Key Laboratory for Structural Chemistry of Unstable and Stable Species, Peking University, Beijing 100871, PR China
[c] State Key Laboratory of Rare Earth Material Chemistry and Application, Peking University, Beijing 100871, PR China
[d] Beijing National Laboratory for Molecular Sciences, Beijing 100871, PR China

ARTICLE INFO

*Keywords:*
Photocatalysis
Dehydrogenation
Surface charge
Activation

ABSTRACT

Carriers generated inside semiconductors during photocatalytic processes are highly energetic and can locally drive reactions that are otherwise difficult or impossible through thermally driven catalysis. However, a model photocatalytic system with high activity and long-term stability is still lacking. Based on surface charge-induced activation, we designed a photocatalytic system of dehydrogenation of methanol and a high activity (95% photon-to-hydrogen efficiency at 405 nm) and long-term durability (still being active after operation for a week) was achieved. The presence of $NiCl_2$ inside the system dramatically changes the adsorption behaviors of reactants and products on catalytic centers and leads to great enhancements in both the catalytic activity and long-term durability of the photocatalyst. This work highlights the importance of electronic property of the surface of catalytic centers for designing efficient and stable photocatalytic systems for solving energy and environment problems.

## 1. Introduction

Photocatalysis utilizing renewable solar energy has emerged as one of the most promising ways to address the environmental-pollution problems and to produce clean energy [1–3]. Photocatalysis has found wide applications in various fields including water splitting [4], carbon dioxide reduction [5,6], nitrogen fixation [7], pollutant decomposition [8] and organic photosynthesis [9]. Although significant progresses have been made in recent decades [10–16], two crucial issues still need to be addressed before industrial applications of photocatalysis, high photocatalytic activity and long-term stability of photocatalysts.

Photon absorption across the solar spectrum (especially the visible light region), separation of charge carriers and the subsequent reaction on the surface hold the key to achieve high photocatalytic activity. To broaden the light absorption range, semiconductors with smaller bandgap are used, but many visible light-responsive photocatalysts exhibit unsatisfactory performance [17–19] as the smaller bandgap inevitably decreases the driving force for chemical reactions [20]. With a suitable bandgap of 2.4 eV, cadmium sulfide (CdS) has attracted enormous interest for its relative high visible light activity [21–23]. To facilitate the charge separation process, constructing heterojunctions either with metals [24,25] or other semiconductors [26–28] is commonly used and a quantum efficiency as high as 93% has been achieved with Pt–PdS/CdS [29]. To accelerate the surface chemical reactions, appropriate co-catalysts are introduced to decrease the overpotential or activation energy [25,30]. Besides, the long-term stability, is another important performance for an applicable photocatalyst [31]. It has been demonstrated that the performance of many photocatalysts, like zinc oxide [32], cuprous oxide [33], deteriorates during photocatalytic processes. The decrease in performance is usually attributed to photocorrosion and suitable carrier scavengers have to be selected to avoid this problem. Moreover, the deactivation of active sites (usually the co-catalysts), which significantly affects the long-term durability of the photocatalysts, was rarely concerned [34].

As is well known, the surface electronic properties play a key role during the catalytic processes through affecting the adsorption/desorption during classical thermal catalysis, and huge successes have been achieved to enhance catalytic activity by tuning the interaction between the supports and the catalysts (electronic metal–support interaction) [35], and the electron density of the metal catalyst during ammonia synthesis [36,37]. As for photocatalysis, the amount (distribution) of electrons/holes above the activation barrier will determine

* Corresponding authors.
*E-mail addresses:* jianghchem@pku.edu.cn (H. Jiang), dsxu@pku.edu.cn (D. Xu).

https://doi.org/10.1016/j.apcatb.2019.117869
Received 30 April 2019; Received in revised form 5 June 2019; Accepted 15 June 2019
Available online 03 July 2019
0926-3373/ © 2019 Elsevier B.V. All rights reserved.

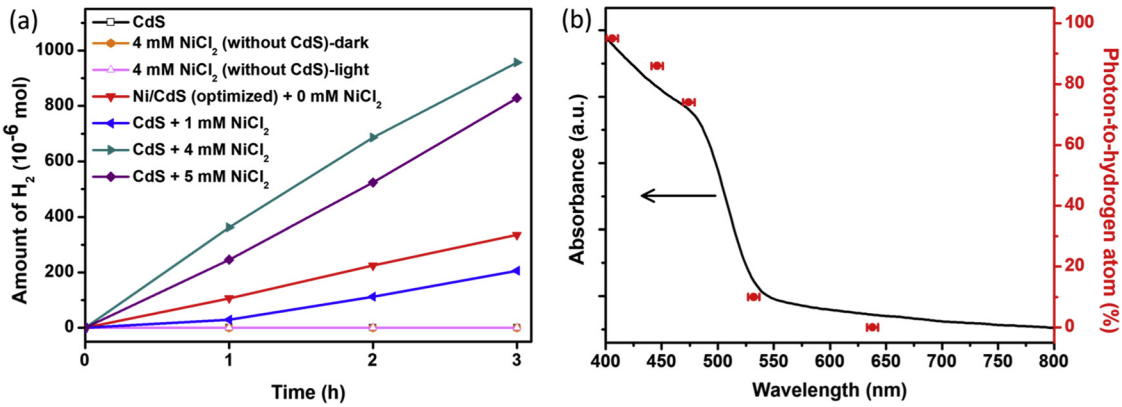


**Fig. 1.** Photocatalytic activity of dehydrogenation of methanol. (a) Time courses of hydrogen evolution with or without $NiCl_2$ under visible light (150 mW/cm$^2$, λ > 420 nm). (b) UV–vis absorption spectrum of the CdS NPs and photon-to-hydrogen atom efficiencies (4 mM $NiCl_2$) under different monochromatic incident lights.

the yield of a photocatalytic reaction. However, the relationship between the reactivity and the electronic properties of the activation center is seldom addressed.

Here, a process based on surface charge-induced activation is designed to improve the efficiency and stability for the photocatalytic dehydrogenation of methanol to produce hydrogen, an ideal clean energy [38]. Unlike the traditional methods, we focus on the relationship between the activity and the electronic properties of the catalytic centers and proposed a novel strategy by regulating the surface charge of catalytic centers to enhance the photocatalytic performance. We successfully tuned the surface charge of the catalytic center under the presence of metallic cations and achieved greatly enhanced photocatalyic activity and long-term durability. In this work, the loading of positive charges on active sites (Ni surface) caused by the presence of nickel chloride ($NiCl_2$), facilitates the adsorption between reactants and catalytic sites and meanwhile promotes desorption of products from the catalytic sites. As a result, the photon-to-hydrogen efficiency up to 95% (at 405 nm) is achieved in a simple photocatalytic system (only requires illumination of $NiCl_2$/methanol solution with CdS nanoparticles), which is the highest efficiency for conversion from photon to hydrogen. At the same time, lowering of the adsorption energy of formaldehydes on the active centers successfully suppresses the poisoning of the catalytic sites, thus the catalysts are still active after continuous operation for 168 h. Furthermore, the oxidized photocatalysts can recover their activity (about 90%) close to the freshly prepared catalysts when being put back to the original photocatalytic system.

## 2. Experimental section

### 2.1. Preparation of photocatalysts

The CdS nanoparticles were prepared by a modified method according to the previous literature [29]. Typically, 160 mL aqueous solution of $Na_2S$ (0.14 M) was added slowly to a 200 mL $Cd(OAc)_2$ solution (0.14 M) under vigorous stirring in 1 h. The mixture was kept stirring for 24 h and then kept without disturbance for 24 h. After filtration and washed with pure water, the resulting yellow mixture was suspended with pure water and transferred to a 100 mL Teflon-lined stainless steel autoclave. Hydrothermal treatment was conducted at 473 K for 72 h. Finally, the yellow product was filtered, washed with water and ethanol, and filtered again, followed by dying under vacuum at 368 K for 24 h.

Ni/CdS nanoparticles were prepared by photodeposition. Typically, a mixture of CdS nanoparticles (6 mg) and 5 mL $NiCl_2$/methanol solution (4 mM) was added into a Schlenk tube (25 mL, Synthware). The mixture was degassed by three freeze-pump-thaw cycles and then illuminated by a 300 W Xe lamp (Microsolar 300, PerfectLight) combined with a UV cut-off filter (λ > 420 nm) for desired different hours with magnetic stirring, followed by washing with methanol under argon atmosphere, drying under vacuum at the room temperature, and kept under argon atmosphere until degassed methanol was added to perform photocatalytic experiments.

### 2.2. Photocatalytic performance test

Photocatalytic dehydrogenation of methanol with Ni/CdS photocatalysts. 5 mL degassed methanol was injected to Ni/CdS nanoparticles (6 mg) in a Schlenk tube (25 mL, Synthware) under argon atmosphere. A water bath was used to keep the tube at 20 ± 1 °C. After freeze-pump-thaw treatment, the reaction mixture was illuminated under visible light (150 mW/cm$^2$, λ > 420 nm) using a 300 W Xe lamp (Microsolar 300, PerfectLight).

Photocatalytic dehydrogenation of methanol with CdS and $NiCl_2$. CdS nanoparticles (6 mg) was mixed with 5 mL $NiCl_2$/methanol solution in a Schlenk tube (25 mL, Synthware) by stirring for several minutes and then degassed by three freeze-pump-thaw cycles. A water bath was used to keep the tube at 20 ± 1 °C. The reaction mixture was illuminated directly under visible light (150 mW/cm$^2$, λ > 420 nm) using a 300 W Xe lamp (Microsolar 300, PerfectLight). For a steady-state system (short-term experiment), a sealed reaction quartz tube was used and all gas products were stored in the headspace. For a flow system, a very tiny iron pipe (with ~1 mm diameter) was used to connect quartz reaction tube of the same type and the U-type gas burette, and evolved gases flowed to the U-type for measurement of the volume.

### 2.3. Products quantification

Two methods were used to determine the quantity of gas evolution, a gas chromatography (GC, Techcomp 7900) with a TDX-01 column for short-term experiments (Fig. 1, Fig. 2b, Figs. S4–S7) and a U-type gas burette for long-term tests (Figs. 2a and c, S10), respectively. Correspondingly, two methods was used to calculate the quantity of $H_2$ (μmol or mmol), the external standard method utilizing the gas chromatography (GC, Techcomp 7900), and the volumetric method as follows:

$$n(H_2) = \frac{V(H_2)}{V_m} \tag{1}$$

$$V_m = \frac{RT}{p} + b - \frac{a}{RT} \tag{2}$$

$V(H_2)$: volume of $H_2$ measured by gas burette (volume of blank experiment has been corrected), mL.

$R$ = 8.3145 Pa·m$^3$ mol$^{-1}$ K$^{-1}$

$T$ = 293.15 K

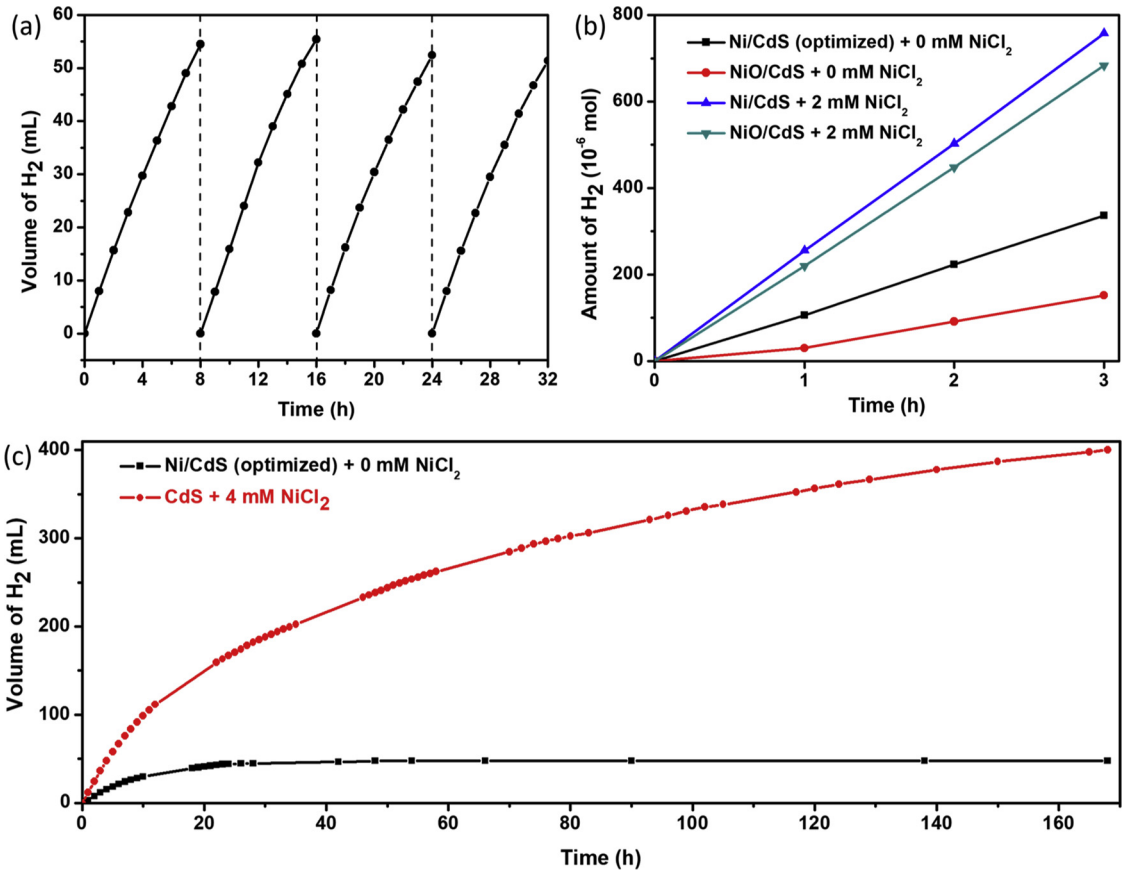


**Fig. 2.** Photocatalytic durability dehydrogenation of methanol. (a) Cyclic performance of photocatalytic reaction with $NiCl_2$ (4 mM, simulated solar light). (b) Regeneration performance by introduction of $NiCl_2$ (2 mM, $\lambda > 420$ nm). (c) Long-term photocatalytic splitting of methanol with or without $NiCl_2$ (150 mW/cm$^2$, $\lambda > 420$ nm).

$p =$ 101,325 Pa
$b = 2.67 \times 10^{-5}\ m^3\ mol^{-1}$
$a = 2.49 \times 10^{-10}\ Pa{\cdot}m^3\ mol^{-2}$

Gas components were also analyzed by the gas chromatography (GC, Techcomp 7900) with argon as the carrier gas and two detectors, thermal conductivity detector (TCD) for $H_2$ and flame ionization detector (FID) for CO, $CO_2$ and $CH_4$. Formaldehyde in methanol solution was determined by a spectrophotometric method (external standard method) utilizing acetylacetone as a derivatization reagent, with a UV/Vis spectrophotometer (Hitachi U-4100).

Measurement of photon-to-hydrogen atom efficiency (PHE). A series of lasers (405, 447, 473, 532 and 637 nm) were used as monochromatic lights. Light power was determined by a laser power meter (Sanwa, LP1).

Photon-to-hydrogen atom efficiency (PHE) was calculated as follows:

$$\mathrm{PHE}\ (\%) = \frac{N_H}{N_i} = \frac{2 \times N(\mathrm{H_2})}{N_i} \times 100\ \% = \frac{2 \times n(\mathrm{H_2}) \times N_A}{Pt/h\nu} \quad (3)$$

where $N_H$ and $N(H_2)$ is number of hydrogen atoms and hydrogen molecules that formed during reaction, $N_c$ is number of photons that converted to hydrogen, $N_i$ is number of incident photons, $n(H_2)$ is mole numbers of hydrogen gas, $N_A$ is the Avogadro constant, $P$ is the power of incident monochromatic light, $t$ is the illumination time, $h$ is the Planck constant, $\upsilon$ is the frequency of incident monochromatic light.

### 2.4. Characterizations

X-ray diffraction (XRD) patterns were obtained on a Rigaku D/max-2500 diffractometer with Cu Kα radiation ($\lambda$ =0.1542 nm) using a current of 100 mA and a voltage of 40 kV. Scan electron microscopy (SEM) images were obtained on a field-emission scanning electron microscope (Merlin Compact) with an accelerating voltage of 5 kV. Transmission electron microscopy (TEM) and high resolution TEM images were obtained on a transmission electron microscope (JEM-2100) and a field-emission high resolution transmission electron microscope (JEM-2100 F). Ultraviolet-visible adsorption reflectance spectrums were collected using a UV/Vis spectrophotometer (Hitachi U-4100) by dispersing the samples in KBr matrix. X-ray photoelectron spectroscopy (XPS) spectrums were collected on an Axis Ultra with a monochromatic Al anode after washing excess $NiCl_2$ in Ar atmosphere and prepare samples in glove box to avoid Ni nanoparticles being oxidized. Inductively coupled plasma-atomic emission spectroscopy (ICP) analysis was conducted on an inductively coupled plasma-atomic emission spectrometer (Prodigy 7) for digestive solution of Ni/CdS which was pre-treated by heating with concentrated nitric acid at 140 °C and diluted with de-ionized water. *In-situ* infrared (IR) experiments were conducted with samples pre-reduced in $H_2$ at 400 °C for 0.5 h, followed by introducing methanol into samples through the continuous bubble method with Ar and pure Ar was used to blow away excess methanol that was not adsorbed tightly on the surface of samples. The zeta potentials of the suspension of CdS, Ni/CdS or Ni nanoparticles dispersed in anhydrous methanol were measured using a temperature-controlled ZetaSizer2000 (Malvern Instruments Ltd.) zeta-potential analyzer. Each sample was measured at least ten times.

### 2.5. Calculation and modeling

Electronic Structure Computational Methods. All calculations reported in this work were performed using the Vienna Ab initio

simulation program (VASP) [39–41]. The core-valence interaction was treated by the projected augmented wave (PAW) method [42]. The exchange and correlation energies were computed using the Perdew, Burke, and Ernzerhof (PBE) [43] generalized gradient approximation (GGA) functional [44]. The cutoff energy for the plane-wave basis was set to 400 eV. Spin-polarized calculations were performed considering the ferromagnetic nature of Ni and the existence of free radicals in the system. To consider dispersion interaction between surfaces and adsorbates, the semiempirical DFT-D3 method proposed by Grimme was exploited [45]. A k-space mesh of 5 × 5 × 1 within the Γ-centered scheme was used to sample the Brillouin zone of the surface unit cell of the (111) surface of Transition Metal and (0001) surface of wurtzite CdS. The conjugate gradient algorithm was used to relax the geometries until the forces on all unconstrained atoms were less than 0.03 eV/Å. For the calculations of the gas phase molecules such as $CH_3OH$ and HCHO, large cubic boxes of 20 × 20 × 20 Å were employed for the geometry optimization of gas-phase molecules. Bader charge analysis was performed to describe the charge transfer between surfaces and adsorbates [46–48].

Surface Models. A 3 × 3 surface slab including four atomic layers was constructed to model the Ni(111) surfaces with 36 metal atoms in each slab. For the (0001) surface of hexagonal wurtzite CdS, we use a 2 × 2 slab including 16 atomic layers with 32 Cd atoms and 32 S atoms in each slab. A vacuum with the thickness of about 15 Å is included to avoid interactions between the repeating slabs. The experimental lattice constants of 3.524 Å for Ni was adopted when building the slab models of transition metal surfaces; for hexagonal wurtzite CdS, lattice constants a = b = 4.137 Å and c = 6.716 Å was used [49]. Half of the atoms in the bottom were fixed in their bulk positions, and the other atoms in the top were allowed to be fully relaxed.

Charged Adsorption. To simulate the Ni nanoparticle with positive charge, which results from the adsorption of $Ni^{2+}$, we built Ni (111) slabs by simply removing one or two electrons from the system. However, for the calculation of the system with periodic boundary conditions, the charge is always compensated with a homogeneous background, which will lead to unphysical electrostatic interaction. Therefore, we adopted the difference between the adsorption energy on charged and neutral slabs to cancel out most of the artificial electrostatic interaction. Along with the results of charge transfer between the adsorbates and surfaces and structure information such as the bond length and bond angle on charged and neutral slabs, we could at least obtain a qualitative picture which can be used to demonstrate the impact of the adsorbed $Ni^{2+}$ in the system.

## 3. Results and discussion

### 3.1. Photocatalytic performance

CdS nanoparticles were employed as light absorption semiconductors. The nanoparticles were prepared through a hydrothermal method [29] and its structures, morphologies and properties are thoroughly characterized (See Supporting Information and Figs. S1–3). Visible light-driven (λ > 420 nm) photocatalytic methanol dehydrogenation with or without $NiCl_2$ was performed at room temperature in a sealed glass tube. All results are shown in Figs. S4 and S5 and some representative results are summarized (Fig. 1a). CdS nanoparticles alone could not exhibit any activity (black line). The photocatalysts (Ni/CdS, photodeposition of Ni on CdS in advance, different Ni loadings were controlled by different time of photodeposition) without $NiCl_2$, showed a moderate activity (red line), which reveals that Ni metals are catalytic centers. When the concentration of $NiCl_2$ reached 2 mM, the rate of hydrogen evolution surpassed that without $NiCl_2$ (Fig. S5). An optimal value was achieved with the concentration increasing to 4 mM (green line). The activity dropped a little with a higher concentration, 5 mM (purple line).

Besides $H_2$, there are some other gas products. However, these by-products are trace gases compared with $H_2$ and the percentages of all the gas products after photoreaction are listed in Table S3. In addition to $H_2$, formaldehyde (HCHO) was the major oxidized liquid product because the molar ratio of HCHO and $H_2$ was approximately 1.0 (Table S4), revealing the stoichiometric manner of photocatalytic dehydrogenation of methanol.

The mechanism for photocatalytic dehydrogenation of alcohols has been discussed in our previous work [12], which may involve the intermediates formed by photo-induced electrons and holes, the Ni-assisted formation of carbonyl (C=O) compounds and the Ni-H hydrides combination into $H_2$. Besides, in our *in-situ* photoreaction system, the photo-induced electrons also take part in the photodeposition of metallic Ni (0) onto CdS surface in the early stage of photoreaction. The reason why CdS alone was totally inactive is still under research in our lab. According to the previous work [12] and preliminary results, the key for this photocatalytic dehydrogenation of alcohols is the interface between Ni and CdS, and the interaction between surface and $CH_3OH$ (Fig. S9).

Under the optimized condition, the photon-to-hydrogen atom efficiency (PHE), which can be used to evaluate the efficiency of converting photons to hydrogen atoms for photocatalytic hydrogen production systems, is quantified (Fig. 1b). The highest value is 95%, achieved at 405 nm (the dynamic curve displayed in Fig. S6), which significantly exceeds the known state-of-the-art level in aqueous systems [29,50–52]. Other results at different wavelengths are also extraordinary, reaching 86% (at 447 nm) and 74% (at 473 nm), respectively. In addition, the photon-to-hydrogen atom efficiencies of $H_2$ evolution correspond well with the absorption spectrum of CdS, which also proves that the dehydrogenation of methanol is a photocatalytic reaction depending on light absorption of CdS.

A practical and robust photocatalytic system should possess a satisfactory recyclability and regeneration performance. Under a simulated solar light, the cyclic reaction system (reaction liquid replaced by fresh $NiCl_2$ methanol solution after every cycle) shows an excellent performance (Fig. 2a). The activity still remained after 4 cycles without obvious decay. Besides, it was also examined that the photocatalyst was deactivated after being exposed to air (red line, Fig. 2b) because some Ni nanoparticles could be oxidized to NiO (similar to Raney Ni). However, when $NiCl_2$ methanol solution with low concentration (2.0 mM) was added, the oxidized photocatalyst (referred to NiO/CdS) regained its activity (recovery of 90%, green line, Fig. 2b) close to that used freshly prepared photocatalyst under the same condition (blue line, Fig. 2b). To further demonstrate the utility of the effect of $NiCl_2$, experiments of visible-light driven dehydrogenation of ethanol (EtOH) with or without $NiCl_2$ were conducted (Fig. S7), which is another important alcohol regarded as a hydrogen storage substrate. The activity of the system with $NiCl_2$ is about 2.5 times of that without $NiCl_2$, which was similar to that using methanol as the reactant.

The long-term photocatalytic hydrogen evolution experiments were performed with visible light in a flow system. 48.2 mmol $h^{-1}$ $g^{-1}$ $H_2$ was achieved during first 24 h (Fig. 2c), which is also the best long-term performance for photocatalytic dehydrogenation of methanol so far. More importantly, the system exhibited a remarkable long-term durability over 168 h and about 400 mL (16.7 mmol) $H_2$ were collected (red line). It is noteworthy that, the long-term performance without $NiCl_2$ was poor (black line), which only produced about 48 mL hydrogen and photocatalysts were fully deactivated after photoreaction for about 54 h.

### 3.2. Characterization of photocatalysts

TEM images of the Ni/CdS nanoparticles (Fig. 3a–c) after reaction for different hours are displayed, corresponding to illumination for 0.5 h, 1.0 h and 3.0 h, respectively. The size of Ni metals increased gradually. A typical high-resolution TEM (HRTEM) image of Ni/CdS after illuminated (Fig. 3d) is displayed. The lattice distance measured

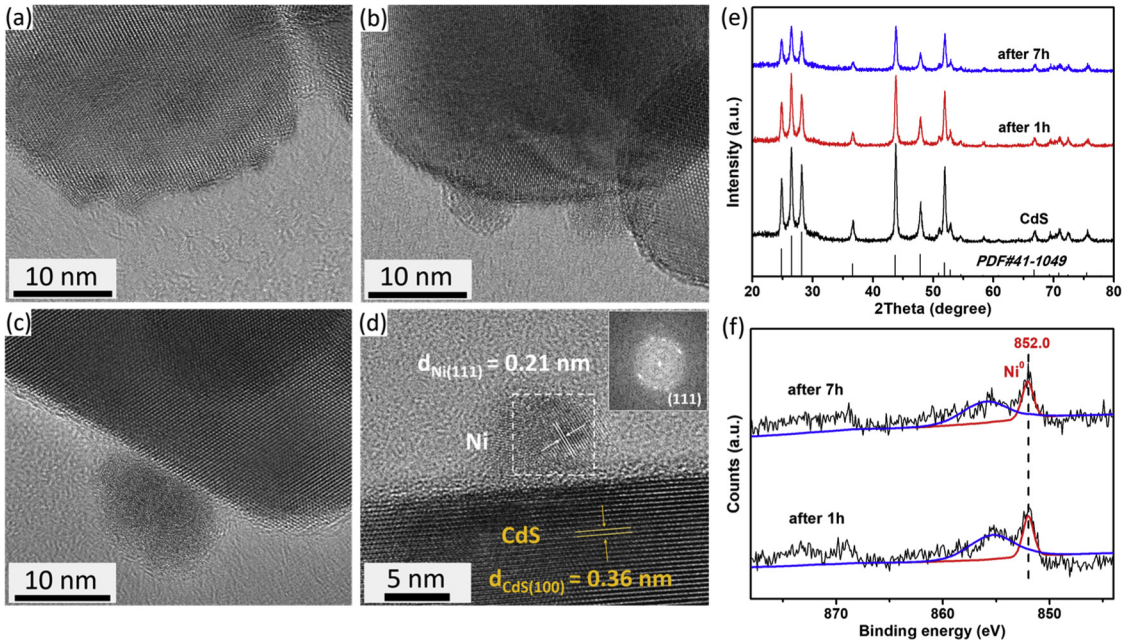


**Fig. 3.** Characterization of photocatalysts after reaction. TEM images of Ni/CdS after reaction for 0.5 h (a), 1.0 h (b) and 3.0 h (c). (d) A typical HRTEM image of Ni/CdS nanoparticle (the inset is the Fourier transform of the marked area). (e) XRD patterns of CdS and Ni/CdS (after illuminated for 1 h and 7 h, respectively). (f) XPS spectrum of elemental Ni from Ni/CdS after reaction for 1 h and 7 h. The vertical line denotes the position of the $Ni^0$ ($2p_{3/2}$) peak. (For interpretation of the references to colour in this figure legend, the reader is referred to the web version of this article).

for the Ni nanocrystal is about 0.21 nm and the diffraction ring in the Fourier transform of the marked area corresponds well with lattice distances of (111) of a metallic Ni (the Powder Diffraction File, PDF#04-0850). The lattice distances measured for the CdS nanoparticle is about 0.36 nm, which corresponds with lattice distances of (100) of CdS (the Powder Diffraction File, PDF#41-1049). Loading amounts of Ni (Fig. S8 and Table S2) also increased under illumination and reached a plateau (less than the initial added amount), which demonstrate that excess $NiCl_2$ existed in the photocatalytic system throughout the whole process. Considering that the activity is similar no matter at the very beginning or after several hours for every reaction with different concentration of $NiCl_2$ (Fig. 1a), the size and loading amount of Ni (Table S1) should not be the key point for activity. Besides, without adding $NiCl_2$, there are some differences between Ni/CdS photocatalysts with different loading amounts of Ni (Fig. S4) but the difference of activity is not significant. This result also demonstrates that the loading amount is not the critical factor.

Photocatalysts remained its original hexagonal crystal form after reaction for 1 h and 7 h without any obvious change of half-peak width in their X-ray diffraction (XRD) patterns (Fig. 3e). Peaks of metallic Ni are hardly found in the XRD patterns (Fig. 3e), which can be attributed to its low loading amount and small crystalline size. Corresponding X-ray photoelectron spectroscopy (XPS) results are displayed (Fig. 3f). The peak at 852.0 eV was attributed to metallic Ni ($2p_{3/2}$), and 855.5 eV was attributed to $NiCl_2$ ($2p_{3/2}$) [50,53] which was only a residual on the surface of the photocatalysts after being washed by methanol because it was difficult to wash $NiCl_2$ completely. No matter after illumination for 1 h or 7 h, the peak of metallic nickel ($Ni^0$) still remained, which reveals that the Ni catalytic centers exist on the surface during the reaction. No peak of NiO is observed in the spectrum since samples were carefully prepared in the glove box.

### 3.3. Adsorption on catalytic centers

To investigate the reason why the additional $NiCl_2$ enhance the photocatalytic dehydrogenation performance, the study on some critical surface catalytic processes, such as the adsorption of reactants and desorption of products on active sites, should be conducted in advance. It is also worthy to note that the photocatalyst (Ni/CdS) without $NiCl_2$ would be completely deactivated after reaction for a period of time (Fig. 2c), which demonstrates that some species may deactivate catalytic centers or active sites. Therefore, more experiments and DFT calculations were conducted to investigate the deactivation on catalytic centers and the effect of $NiCl_2$. As mentioned above, CdS without Ni deposition could not show any activity, definitely metallic Ni deposited on CdS is the catalytic center. Besides, *in-situ* infrared (IR) results (Fig. S9) revealed that $CH_3OH$ adsorbed on Ni/CdS surface have two strong bands, 1567 $cm^{-1}$ and 1435 $cm^{-1}$ (OH deformation), which are extremely weaker on bare CdS surface. This result also reveals that $CH_3OH$ may have a stronger interaction with metallic Ni compared with CdS.

We have proved that HCHO was the final oxidized product no matter with or without $NiCl_2$ (Table S4). Therefore, we considered whether HCHO would deactivate Ni catalytic centers or not, since another study has reported that the posion of catalysts via adsorption of the aldehyde products in thermal catalysis [54]. The adsorption behavior of the product (HCHO) over the Ni(111) surface by the DFT method was investigated and compared with that of the reactant ($CH_3OH$). The adsorption energy of HCHO is larger than that of $CH_3OH$ (on the top of Fig. 4a), which reveals the adsorption of HCHO is much more stable than that of $CH_3OH$ on the Ni surface [34]. Therefore, we considered that, HCHO has a poisoning effect on Ni active sites, preventing $CH_3OH$ from approaching the Ni surface, thus reducing the probability of interaction between reactants and active sites, leading to the deactivation of Ni/CdS, which is similar to other poisoning results in photocatalysis [34], electrocatalysis [55] and thermal catalysis [54]. Moreover, the activity recovered to a certain degree after the ultrasonic treatment (Fig. S10), which also demonstrated that removing adsorbed HCHO on the catalytic surface could decrease deactivation. However, the activity declined quickly again just after several hours, since HCHO always existed in the system. Besides, cyclic experiment results (Fig. 2a) also demonstrated that the initial activity recovered by removing HCHO generated in every cycle.

Different adsorption structures between $CH_3OH$ and HCHO (on the

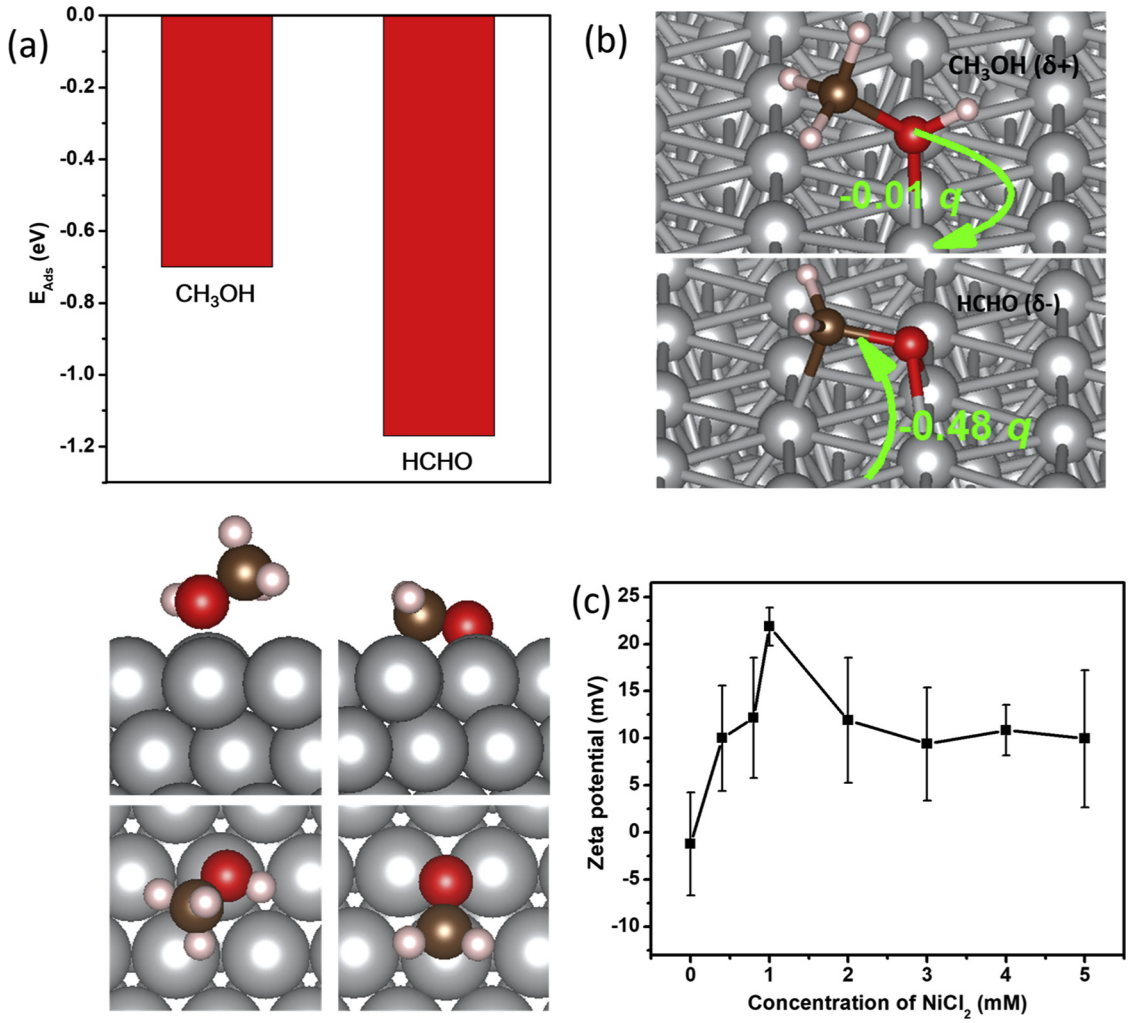


**Fig. 4.** Adsorption of species on active sites. (a) *In-situ* IR spectra of adsorbed methanol on CdS and Ni/CdS (Inset: adsorption energies of $CH_3OH$ on Ni and CdS surface). (b) Variable temperature infrared experiment of adsorbed methanol on Ni/CdS. (c) Adsorption energies and structures of $CH_3OH$ and HCHO at Ni surface.

bottom of Fig. 4a, $CH_3OH$ adsorbed on the Ni surface via oxygen atom of alcohol O—H group and HCHO via both oxygen atom and carbon atom of C═O bond) always demonstrate different charge transfer manners between adsorbed species and Ni surface. Moreover, Bader charge analysis was also performed to calculate the net charge of adsorbed species (Fig. 4b, Table S5), revealing the charge transfer between the surface and adsorbates. According to calculation results, electrons would transfer from $CH_3OH$ to Ni but transfer from Ni to HCHO (Fig. 4b). From the perspective of coordination chemistry, $CH_3OH$ and HCHO could be regarded as a weak π-donor and π-acceptor, respectively. That is to say, if the surface of catalytic centers is endowed with extra charges, the adsorption of $CH_3OH$ and HCHO will change differently, which is possible to affect their interaction with Ni surface and thus the photocatalytic performance.

We measured the zeta potential of different dispersion systems. No matter for CdS or Ni/CdS nanoparticles, while dispersed in $NiCl_2$/$CH_3OH$ solution, the zeta potential was more positive than that without $NiCl_2$ (Fig. S11), which demonstrated that $Ni^{2+}$ could be adsorbed on the Ni/CdS or CdS surface. In order to exclude the influence of CdS, we further performed zeta potential measurement on Ni nanoparticles with $NiCl_2$/$CH_3OH$ solution (Fig. 4c). From 0 to 5 mM, zeta potential firstly increased (becomes more positive) and then decreased. Anyhow, when $NiCl_2$ was added, values of zeta potential presented an increasing trend towards the positive direction. This phenomenon may be ascribed to the specific adsorption of positive $Ni^{2+}$ on metallic Ni surface, which has been stated in Fajan's rule (ions with the same chemical elements as colloidal particles can be preferentially absorbed). When the concentration of $NiCl_2$ increases, the adsorption of $Ni^{2+}$ makes solvation layers have more positive ions and the zeta potential increased. However, excess positive ions diffusing into the solvation layer results in decrease of zeta potential. Theoretically, zeta potential results (positive/negative) provide indicative evidences that the predominant ions in the electronic double layer are similar (positive/negative) [56]. It is worthy to note that the zeta potential of Ni metal surface with excess $NiCl_2$ under light condition is close to that under dark condition because the process of photoreduced $Ni^{2+}$ to Ni became very slow and was almost negligible after a period of time (Fig. S8). Therefore, these results could disclose the surface charge of Ni during photoreaction at least qualitatively.

### 3.4. Activation mechanism

Based on results above, we tentatively considered that, the poisoning of active sites in the photocatalytic system is suppressed or weakened with excess $NiCl_2$ ($Ni^{2+}$), leading to a higher activity and enhanced durability. The DFT method was again used to verify this hypothesis. Total charge of Ni, 0, +1 and +2, were used to represent Ni surface with different positive charges.

We used the difference between the adsorption energy of $CH_3OH$ and HCHO (Fig. 5a), [$\Delta E_{Ads} = E_{Ads}(CH_3OH) - E_{Ads}(HCHO)$], to evaluate

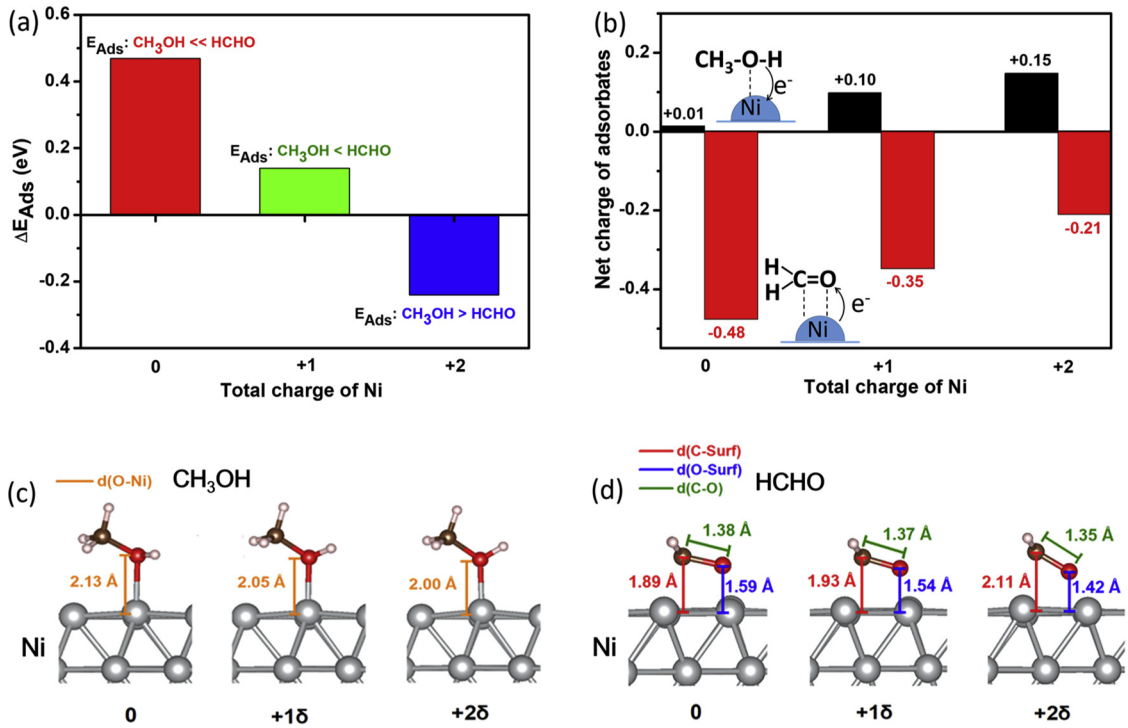


**Fig. 5.** DFT calculations of adsorption on charged surface of the catalytic center. (a) $\Delta E_{ads}$ with different charges of Ni surface. (b) Net charges of adsorbed species with different charges of Ni surface. Variation of adsorption structures of $CH_3OH$ (c) and HCHO (d) on Ni surfaces with different charges.

the effects of surface charging, since absolute values of adsorption energy on charged surfaces can suffer from the uncertainty related to unphysical electrostatic interaction between surface charges and the compensating background charges. $\Delta E_{Ads}$ decreases from 0.47 eV to 0.14 eV and −0.24 eV, which demonstrates that, with the charge of Ni surface becoming more positive, the relative stability of reactant and product adsorption changes significantly, and the adsorption of $CH_3OH$ becomes stronger while that of HCHO becomes weaker.

The variation trend of net charge for $CH_3OH$ and HCHO is similar (Fig. 5b, Table S5), both become more positive with total charge becoming more positive. According to different adsorption manners between $CH_3OH$ and HCHO mentioned above (Fig. 4a and b), more electrons would flow from $CH_3OH$ to Ni, however HCHO accepts less electrons. Thus, more electrons take part in the interaction between $CH_3OH$ and Ni, but less for HCHO, which also demonstrates the adsorption of $CH_3OH$ becomes stronger and the adsorption of HCHO becomes weaker.

To further verify the conclusion above, the structures of adsorbed $CH_3OH$ and HCHO were investigated as well. As for $CH_3OH$ (Fig. 5c), d (O-Ni) becomes shorter and shorter from 2.13 Å to 2.05 Å and 2.00 Å, which demonstrates the interaction between $CH_3OH$ and Ni becomes stronger with total charge of Ni getting more positive. However, it is totally different for HCHO. d(C-surf) increases from 1.89 Å to 1.93 Å and 2.11 Å, but d(O-surf) decreases from 1.59 Å to 1.54 Å and 1.42 Å (Fig. 5d). Meanwhile, d(C-O) decreases from 1.38 Å to 1.37 Å and 1.35 Å. This result reveals that HCHO is gradually deviating from its most stable adsorbed structure and the adsorption is weakened due to positive charging of Ni surface.

As mentioned above, in the experiment of regeneration of photocatalysts by introduction of $NiCl_2$, the activity could almost recover (Fig. 2b). Since Ni/CdS or partially oxidized Ni/CdS employed in this experiment was prepared in advance by illumination for 9 h (photodeposition was almost complete), newly added $Ni^{2+}$ was hardly again reduced to Ni by photo-generated electrons. Therefore, the increased and recovered activity could be ascribed to the poisoning suppression effect the activation of catalytic centers by $NiCl_2$.

Based on all the results above, we propose a new activation mechanism, surface charge-induced activation of catalytic centers, for the enhanced activity and increased durability in photocatalytic dehydrogenation of methanol. With excess $Ni^{2+}$ adsorbed on Ni, the surface potential becomes more positive (more positive charges are loaded on Ni surface), which promotes the adsorption of $CH_3OH$ and meanwhile facilitates desorption of HCHO, leading to stronger interaction between reactants and active sites, and weaker for the products. Thus, the rate of adsorption and activation for $CH_3OH$ will increase, and meanwhile the rate of HCHO leaving actives sites will increase. In other words, positively charged Ni surface via excess $Ni^{2+}$ adsorption suppresses poisoning effect from HCHO products, leading to a higher activity and longer durability.

## 4. Conclusion

In summary, we successfully developed a highly efficient, robust and stable photocatalytic methanol dehydrogenation system through regulating the surface charge of catalytic centers. An ultrahigh photon-to-hydrogen atom efficiency and greatly enhanced long-term durability was obtained, which exceeded state-of-the-art values ever reported. Based on DFT modeling, we proposed that surface charge-induced activation on active sites through adsorption of $Ni^{2+}$ could suppresse poisoning of catalytic sites. The adsorption of $Ni^{2+}$ on catalytic centers leading to positively charged Ni surface, which effectively promotes the adsorption of $CH_3OH$ and desorption of HCHO, thus keeping the active centers active and decreasing deactivation. We believe that this study will provide a novel and unique strategy for boosting the activity and long-term stability in photocatalysis by modulating the surface charge on catalytic centers. Also, this work provides a very promising strategy for hydrogen production and chemical industry.

## Conflict of interest

The authors declare no competing interests.

## Acknowledgements

We thank X. Wang for help with zeta potential measurement; M. Zeng, X. Deng, S. Feng, A. Muhetaer, and J. Tian for help with experimental operation of photocatalysis; X. Liu for help with ICP measurement; L. Yang for help with TEM characterization. Z. Zhang and Y. Yang for help with text proofreading. We thank Analytical Instrumentation Center of Peking University for providing instruments and operation for photocatalysts characterization. Funding: This research was financially supported by the National Natural Science Foundation of China (grant No. 21821004) and the National Basic Research Program of China (Nos. 2014CB239303).

## Appendix A. Supplementary data

Supplementary material related to this article can be found, in the online version, at doi:https://doi.org/10.1016/j.apcatb.2019.117869.

## References

[1] X. Chen, S. Shen, L. Guo, S.S. Mao, Semiconductor-based photocatalytic hydrogen generation, Chem. Rev. 110 (2010) 6503–6570.
[2] H. Tong, S. Ouyang, Y. Bi, N. Umezawa, M. Oshikiri, J. Ye, Nano-photocatalytic materials: possibilities and challenges, Adv. Mater. 24 (2012) 229–251.
[3] F.F. Wang, Q. Li, D.S. Xu, Recent progress in semiconductor-based nanocomposite photocatalysts for solar-to-chemical energy conversion, Adv. Energy Mater. 7 (2017) 1700529.
[4] S.S. Chen, T. Takata, K. Domen, Particulate photocatalysts for overall water splitting, Nat. Rev. Mater. 2 (2017) 17050.
[5] S.N. Habisreutinger, L. Schmidt-Mende, J.K. Stolarczyk, Photocatalytic reduction of $CO_2$ on $TiO_2$ and other semiconductors, Angew. Chem. Int. Ed. Engl. 52 (2013) 7372–7408.
[6] R. Shi, G.I. Waterhouse, T. Zhang, Recent progress in photocatalytic $CO_2$ reduction over perovskite oxides, Solar RRL 1 (2017) 1700126.
[7] X.Z. Chen, N. Li, Z.Z. Kong, W.J. Ong, X.J. Zhao, Photocatalytic fixation of nitrogen to ammonia: state-of-the-art advancements and future prospects, Mater. Horiz. 5 (2018) 9–27.
[8] C. Chen, W. Ma, J. Zhao, Semiconductor-mediated photodegradation of pollutants under visible-light irradiation, Chem. Soc. Rev. 39 (2010) 4206–4219.
[9] J.M. Narayanam, C.R. Stephenson, Visible light photoredox catalysis: applications in organic synthesis, Chem. Soc. Rev. 40 (2011) 102–113.
[10] Z. Zou, J. Ye, K. Sayama, H. Arakawa, Direct splitting of water under visible light irradiation with an oxide semiconductor photocatalyst, Nature 414 (2001) 625.
[11] X. Wang, K. Maeda, A. Thomas, K. Takanabe, G. Xin, J.M. Carlsson, K. Domen, M. Antonietti, A metal-free polymeric photocatalyst for hydrogen production from water under visible light, Nat. Mater. 8 (2009) 76–80.
[12] Z. Chai, T.T. Zeng, Q. Li, L.Q. Lu, W.J. Xiao, D. Xu, Efficient visible light-driven splitting of alcohols into hydrogen and corresponding carbonyl compounds over a Ni-modified CdS photocatalyst, J. Am. Chem. Soc. 138 (2016) 10128–10131.
[13] T. Haas, R. Krause, R. Weber, M. Demler, G. Schmid, Technical photosynthesis involving $CO_2$ electrolysis and fermentation, Nat. Catal. 1 (2018) 32–39.
[14] H. Yu, R. Shi, Y. Zhao, T. Bian, Y. Zhao, C. Zhou, G.I. Waterhouse, L.Z. Wu, C.H. Tung, T. Zhang, Alkali-assisted synthesis of nitrogen deficient graphitic carbon nitride with tunable band structures for efficient visible-light-driven hydrogen evolution, Adv. Mater. 29 (2017) 1605148.
[15] Y. Zhao, Y. Zhao, G.I. Waterhouse, L. Zheng, X. Cao, F. Teng, L.Z. Wu, C.H. Tung, D. O'Hare, T. Zhang, Layered-double-hydroxide nanosheets as efficient visible-light-driven photocatalysts for dinitrogen fixation, Adv. Mater. 29 (2017) 1703828.
[16] Y. Zhao, Z. Li, M. Li, J. Liu, X. Liu, G.I. Waterhouse, Y. Wang, J. Zhao, W. Gao, Z. Zhang, Reductive transformation of layered-double-hydroxide nanosheets to Fe-based heterostructures for efficient visible-light photocatalytic hydrogenation of CO, Adv. Mater. 30 (2018) 1803127.
[17] K. Maeda, T. Takata, M. Hara, N. Saito, Y. Inoue, H. Kobayashi, K. Domen, GaN: ZnO solid solution as a photocatalyst for visible-light-driven overall water splitting, J. Am. Chem. Soc. 127 (2005) 8286–8287.
[18] W.J. Jo, H.J. Kang, K.-J. Kong, Y.S. Lee, H. Park, Y. Lee, T. Buonassisi, K.K. Gleason, J.S. Lee, Phase transition-induced band edge engineering of $BiVO_4$ to split pure water under visible light, Proc. Natl. Acad. Sci. 112 (2015) 13774–13778.
[19] Z. Wang, Y. Inoue, T. Hisatomi, R. Ishikawa, Q. Wang, T. Takata, S. Chen, N. Shibata, Y. Ikuhara, K. Domen, Overall water splitting by $Ta_3N_5$ nanorod single crystals grown on the edges of $KTaO_3$ particles, Nat. Catal. 1 (2018) 756–763.
[20] F. Wang, Y. Huang, Z. Chai, M. Zeng, Q. Li, Y. Wang, D. Xu, Photothermal-enhanced catalysis in core-shell plasmonic hierarchical $Cu7S_4$ microsphere@zeolitic imidazole framework-8, Chem. Sci. 7 (2016) 6887–6893.
[21] Z. Chai, Q. Li, D. Xu, Photocatalytic reduction of $CO_2$ to CO utilizing a stable and efficient hetero–homogeneous hybrid system, RSC Adv. 4 (2014) 44991–44995.
[22] K.A. Brown, D.F. Harris, M.B. Wilker, A. Rasmussen, N. Khadka, H. Hamby, S. Keable, G. Dukovic, J.W. Peters, L.C. Seefeldt, Light-driven dinitrogen reduction catalyzed by a CdS: nitrogenase MoFe protein biohybrid, Science 352 (2016) 448–450.
[23] C.M. Wolff, P.D. Frischmann, M. Schulze, B.J. Bohn, R. Wein, P. Livadas, M.T. Carlson, F. Jäckel, J. Feldmann, F. Würthner, J.K. Stolarczyk, All-in-one visible-light-driven water splitting by combining nanoparticulate and molecular co-catalysts on CdS nanorods, Nat. Energy 3 (2018) 862–869.
[24] J. Yang, H. Yan, X. Wang, F. Wen, Z. Wang, D. Fan, J. Shi, C. Li, Roles of cocatalysts in Pt–PdS/CdS with exceptionally high quantum efficiency for photocatalytic hydrogen production, J. Catal. 290 (2012) 151–157.
[25] J. Ran, J. Zhang, J. Yu, M. Jaroniec, S.Z. Qiao, Earth-abundant cocatalysts for semiconductor-based photocatalytic water splitting, Chem. Soc. Rev. 43 (2014) 7787–7812.
[26] K. Maeda, Z-Scheme Water Splitting Using Two Different Semiconductor Photocatalysts, ACS Catal. 3 (2013) 1486–1503.
[27] P. Zhou, J. Yu, M. Jaroniec, All-solid-state Z-scheme photocatalytic systems, Adv. Mater. 26 (2014) 4920–4935.
[28] H. Zhao, X. Ding, B. Zhang, Y. Li, C. Wang, Enhanced photocatalytic hydrogen evolution along with byproducts suppressing over Z-scheme $Cd_xZn_{1-x}S$/Au/g-$C_3N_4$ photocatalysts under visible light, Sci. Bull. 62 (2017) 602–609.
[29] H. Yan, J. Yang, G. Ma, G. Wu, X. Zong, Z. Lei, J. Shi, C. Li, Visible-light-driven hydrogen production with extremely high quantum efficiency on Pt–PdS/CdS photocatalyst, J. Catal. 266 (2009) 165–168.
[30] J. Yang, D. Wang, H. Han, C. Li, Roles of cocatalysts in photocatalysis and photoelectrocatalysis, Acc. Chem. Res. 46 (2013) 1900–1909.
[31] L. Pan, J.H. Kim, M.T. Mayer, M.-K. Son, A. Ummadisingu, J.S. Lee, A. Hagfeldt, J. Luo, M. Grätzel, Boosting the performance of $Cu_2O$ photocathodes for unassisted solar water splitting devices, Nat. Catal. 1 (2018) 412–420.
[32] A. Kudo, Y. Miseki, Heterogeneous photocatalyst materials for water splitting, Chem. Soc. Rev. 38 (2009) 253–278.
[33] A. Paracchino, V. Laporte, K. Sivula, M. Gratzel, E. Thimsen, Highly active oxide photocathode for photoelectrochemical water reduction, Nat. Mater. 10 (2011) 456–461.
[34] G. Han, Y.H. Jin, R.A. Burgess, N.E. Dickenson, X.M. Cao, Y. Sun, Visible-light-driven valorization of biomass intermediates integrated with $H_2$ production catalyzed by ultrathin Ni/CdS nanosheets, J. Am. Chem. Soc. 139 (2017) 15584–15587.
[35] C.T. Campbell, Catalyst–support interactions: electronic perturbations, Nat. Chem. 4 (2012) 597.
[36] A. Ozaki, Development of alkali-promoted ruthenium as a novel catalyst for ammonia synthesis, Acc. Chem. Res. 14 (1981) 16–21.
[37] H. Bielawa, O. Hinrichsen, A. Birkner, M. Muhler, The ammonia-synthesis catalyst of the next generation: barium-promoted oxide-supported ruthenium, Angew. Chem. Int. Ed. 40 (2001) 1061–1063.
[38] L. Schlapbach, A. Züttel, Hydrogen-storage materials for mobile applications, Nature 414 (6861) (2011) 353–358.
[39] G. Kresse, J. Furthmüller, Efficient iterative schemes for ab initio total-energy calculations using a plane-wave basis set, Phys. Rev. B 54 (1996) 11169.
[40] G. Kresse, J. Hafner, Ab initio molecular dynamics for liquid metals, Phys. Rev. B 47 (1993) 558.
[41] G. Kresse, J. Hafner, Norm-conserving and ultrasoft pseudopotentials for first-row and transition elements, J. Phys. Condens. Matter 6 (1994) 8245.
[42] P.E. Blöchl, Projector augmented-wave method, Phys. Rev. B 50 (1994) 17953.
[43] J.P. Perdew, K. Burke, M. Ernzerhof, Generalized gradient approximation made simple, Phys. Rev. Lett. 77 (1996) 3865.
[44] J.P. Perdew, J.A. Chevary, S.H. Vosko, K.A. Jackson, M.R. Pederson, D.J. Singh, C. Fiolhais, Atoms, molecules, solids, and surfaces: applications of the generalized gradient approximation for exchange and correlation, Phys. Rev. B 46 (1992) 6671.
[45] S. Grimme, S. Ehrlich, L. Goerigk, Effect of the damping function in dispersion corrected density functional theory, J. Comput. Chem. 32 (2011) 1456–1465.
[46] W. Tang, E. Sanville, G. Henkelman, A grid-based Bader analysis algorithm without lattice bias, J. Phys.: Condens. Matter 21 (2009) 084204.
[47] E. Sanville, S.D. Kenny, R. Smith, G. Henkelman, Improved grid-based algorithm for Bader charge allocation, J. Comput. Chem. 28 (2007) 899–908.
[48] G. Henkelman, A. Arnaldsson, H. Jónsson, A fast and robust algorithm for Bader decomposition of charge density, Comp. Mater. Sci. 36 (2006) 354–360.
[49] C.-Y. Yeh, Z. Lu, S. Froyen, A. Zunger, Zinc-blende–wurtzite polytypism in semiconductors, Phys. Rev. B 46 (1992) 10086.
[50] T. Simon, N. Bouchonville, M.J. Berr, A. Vaneski, A. Adrovic, D. Volbers, R. Wyrwich, M. Doblinger, A.S. Susha, A.L. Rogach, F. Jackel, J.K. Stolarczyk, J. Feldmann, Redox shuttle mechanism enhances photocatalytic $H_2$ generation on Ni-decorated CdS nanorods, Nat. Mater. 13 (2014) 1013–1018.
[51] X.-B. Li, Y.-J. Gao, Y. Wang, F. Zhan, X.-Y. Zhang, Q.-Y. Kong, N.-J. Zhao, Q. Guo, H.-L. Wu, Z.-J. Li, Self-assembled framework enhances electronic communication of ultrasmall-sized nanoparticles for exceptional solar hydrogen evolution, J. Am. Chem. Soc. 139 (2017) 4789–4796.
[52] S. Guan, X. Fu, Y. Zhang, Z. Peng, β-NiS modified CdS nanowires for photocatalytic $H_2$ evolution with exceptionally high efficiency, Chem. Sci. 9 (2018) 1574–1585.
[53] Y. Coffinier, N. Nguyen, H. Drobecq, O. Melnyk, V. Thomy, R. Boukherroub, Affinity surface-assisted laser desorption/ionization mass spectrometry for peptide enrichment, Analyst 137 (2012) 5527–5532.
[54] T.L. Lohr, A.R. Mouat, N.M. Schweitzer, P.C. Stair, M. Delferro, T.J. Marks, Efficient catalytic greenhouse gas-free hydrogen and aldehyde formation from aqueous alcohol solutions, Energy Environ. Sci. 10 (2017) 1558–1562.
[55] J. Baschuk, X. Li, Carbon monoxide poisoning of proton exchange membrane fuel cells, Int. J. Energy Res 25 (2001) 695–713.
[56] S. Bhattacharjee, DLS and zeta potential–what they are and what they are not? J. Control. Release 235 (2016) 337–351.